Direct Laser Metal Deposition of AISI H13 Cladding on Copper–Beryllium Alloy Substrate Through a Stainless-Steel Buffer Layer Strategy

Zhao Zhao,* Matteo Perini, Paolo Bosetti, and Massimo Pellizzari

AISI H13 cladding is deposited on the copper–beryllium (CuBe) alloy substrate by direct laser metal deposition via a buffer layer strategy. The SS316L austenite stainless steel is used as the buffer material attempting to reduce the risk of cracking. Single- and multi-layer samples are deposited, including single-layer SS316L, 1-layer SS316L + 1-layer H13, 2-layers SS316L + 1-layer H13, and 1-layer SS316L + 4-layers H13. The defect-free single-layer SS316L cladding is successfully deposited after the parameter pre-optimization. Two types of defects including porosity and cracking are observed in all multi-layer systems. The cladding microhardness of the 2-layer system is rather low (400HV). A 50% increase in the cladding microhardness is observed when depositing on the five-layer system. The five-layer system shows a better load-bearing capability (LBC) compared with the CuBe substrate in the low loading range. As load increases above 10 kN, the five-layer cladding system shows the worse LBC compared to CuBe due to the low strength of the heat-affected zone. A 2.7% cladding to substrate thickness ratio allows keeping more than 80% of the original thermal conductivity of the CuBe substrate.

1. Introduction

In the injection molding industry, almost of molds are currently made from single materials including steel, aluminum alloy, and copper–beryllium (CuBe) alloy. Steel molds have a long lifespan but cannot be used in situations that need fast heat removal.[1] CuBe alloys can remarkably reduce the injection molding cycle times due to their high electrical and thermal conductivity (TC).[2] However, their relatively low strength and wear resistance make it easy to suffer from surface damage during service. To achieve a

Z. Zhao, P. Bosetti, M. Pellizzari
Department of Industrial Engineering
University of Trento
Via Sommarive 9, 38123 Trento, Italy
E-mail: zhao.zhao@unitn.it

M. Perini
Trentino Sviluppo Spa
PROM Facility
Via Fortunato Zeni 8, 38068 Rovereto, Italy

The ORCID identification number(s) for the author(s) of this article can be found under https://doi.org/10.1002/srin.202200387.

long lifespan and high productivity in one mold simultaneously, bimetallic molds are strongly attractive in academic and industrial communities. One possible route is to deposit a hard coating on CuBe molds' surfaces, to provide sufficient load-bearing capability (LBC) meanwhile keep the relatively high TC of a whole mold.[3] Conventional technologies such as physical or chemical vapor deposition can only produce relatively thin films ($<10\,\mu m$), which do not permit achieving this goal.[4] Meanwhile, these are also relatively not cost-effective and quite time-consuming.

Direct laser metal deposition (DLMD) is one of the additive manufacturing (AM) technologies that have been developed for decades.[5,6] It is also well known as laser cladding (LC) if it is applied to the coating deposition process. A high-energy source beam is radiated onto the surface of the working piece and the powder is coaxially or sidely fed into the molten pool to deposit a part layer by layer. With the aid of a multi-material feeding system, two or more materials can be deposited at the same time thus allowing alloying.[7–9] Moreover, by DLMD thick coatings can be deposited up to several millimeters thick faster compared with other techniques.[4,5] Combined with its flexibility and automated production process, DLMD is appropriate to improve the surface hardness of tools and dies.

Hot work tool steel is a suitable coating material to increase the hardness and wear resistance of copper alloys.[10] However, a steel–copper alloy bimetallic structure faces many challenges. First, the mismatch of thermal properties such as coefficient of thermal expansion (CTE) between steel and copper alloy results in residual thermal stress, which contributes to crack formation. In addition, the high reflectivity of copper alloys concerning the infrared laser requires much higher laser power which may induce machine damage by reflected laser radiation.[11] According to the authors' previous work, depositing H13 cladding directly on CuBe is inappropriate since cracks can be hardly removed by parameter optimization.[12] The first attempt done by the authors for avoiding cracks was to apply the substrate preheating just before deposition. 150 °C preheating helped produce crack-free parts. However, the CuBe substrate was softened due to the over-aging induced by preheating, even though the softening is within a tolerable range from an industrial point of view. Another drawback of using preheating to suppress cracking is

**ADVANCED
SCIENCE NEWS**

www.advancedsciencenews.com

**steel
research**
international

www.steel-research.de

that it is not always easy to preheat large-size molds. Moreover, the role of preheating on cracking elimination was unclear since it reduces thermal stress and meanwhile avoids the martensite transformation circles during deposition. Therefore, other methods were proposed to solve the aforementioned issues and reveal the cracking mechanism. For example, adding a third-material intermediate layer between the tool steel and copper alloy could be a solution since a material with intermediate properties can play as a "buffer" zone to reduce the mismatch of properties between two base materials.[13] Imran et al. used SS316 and 41C SS stainless steel as a buffer between H13 coating and CuBe substrate.[10,14] However, the defects including cracking and porosity in as-built specimens were not discussed in detail. Zhang et al. deposited pure Cu cladding on SS304L and H13 substrate by DLMD via a high-Ni-content Ni-based alloy buffer.[15,16] No crack was observed in cladding, which may result from the stable solid solution of Ni with Cu. In this work, an austenitic stainless steel grade, namely SS316L, was chosen as a buffer. The buffer selection was based on the following considerations. First, its CTE is in between H13 and CuBe ($CTE_{H13} = 11 \times 10^{-6}$, $CTE_{SS316L} = 16 \times 10^{-6}$, $CTE_{CuBe1.9} = 17 \times 10^{-6} \, K^{-1}$), which reduces the thermal stress during deposition. Meanwhile, it does not undergo any phase transformation during deposition, which helps to investigate the cracking mechanism by combining the observations from the previous work.[12] Moreover, SS316L is more ductile than H13 and CuBe, thus playing as a "mechanical buffer" with respect to any process-induced stress. Considering all factors mentioned earlier, SS316L may be a suitable candidate as an intermediate layer between H13 and CuBe.

In this work, the H13 tool steel cladding was deposited on a CuBe alloy substrate using DLMD through a buffer layer strategy. Different SS316L-based buffer layers were chosen as buffer material, considering single-layer as well as multi-layer buffers. The microstructure of claddings was characterized, and their chemical composition profile was probed by energy dispersive spectrometry. The microhardness, LBC, and TC were measured.

2. Experimental Section

AISI H13 powder produced by the gas atomization process was provided by Sandvik Osprey. The particle size was uniform, with about 94.76% of powders in a range between 45 and 106 μm. The gas atomized SS316L powder supplied by MIMETE involved 80% of particles in the range between 45 and 106 μm. The CuBe base plate (Uddeholm Moldmax HH) with a size of $100 \times 100 \times 20 \, mm$ was used as substrate. Plates, 20 mm in thickness, were delivered in the aged condition, with a starting hardness of 400 HV ± 10. The chemical composition of the three materials used is listed in **Table 1**. Metallographic cross-sections normal to the deposition direction were obtained by precision cutting using a diamond blade and conventional metallographic preparation with grinding papers and final mirror polishing with diamond pastes down to 3 μm.

A Lasertec 65 3D hybrid DLMD machine (DMG Mori) was used with a laser wavelength of 1020 nm. A laser beam with a diameter of 3 mm was perpendicularly focused on the workpiece surface. Argon gas was used for the molten pool protection and

Table 1. Nominal composition of the materials used in this article (wt%).

Material	Fe	Cr	Ni	Mn	Mo	V	Si	C	Cu	Co	Be
H13	Bal.	5.2	–	0.5	1.6	1.1	1.0	0.4	–	–	–
SS316L	Bal.	17.5	12.5	2.0	2.2	–	0.75	0.03	0.75	–	–
CuBe	–	–	0.3	–	–	–	–	–	Bal.	0.3	1.9

Table 2. Structure of the claddings investigated.

Sample order	Substrate	SS316 layer No.	H13 layer No.	Total layer No.
S1	CuBe	1	0	1
S2	CuBe	1	1	2
S3	CuBe	2	1	3
S4	CuBe	1	4	5

powder carrier, with a flow rate of 5 and 5.5 L min⁻¹ separately. The processing parameters were pre-optimized to minimize defects in the cladding. Note that considering the cracking is more detrimental than porosity, the parameter optimization mainly focused on the cracking elimination. The parameter combination after optimization was utilized and kept constant for each layer of all samples, which are: laser power 2200 W, scan speed 600 mm min⁻¹, powder feed rate 3.3 g min⁻¹, and overlap ratio 50%. The cladding area was $15 \times 15 \, mm^2$. Four samples were chosen for analysis (**Table 2**). The geometrical features including the cladding thickness, cladding area, and melted substrate area were measured by the software ImageJ. The cladding thickness of each sample is the mean of ten values. The illustration of geometrical features was shown in **Figure 1**. The one-layer thickness of SS316L was measured from the single-layer SS316L sample S1. Meanwhile, the thickness of single-layer SS316L was assumed to be constant in multi-layer samples since the parameters for each layer remained the same. The H13 cladding thickness was calculated by the SS316L cladding thickness subtracted from the total cladding thickness. Note that the penetration depth induced by the melting of substrate or previous layers is not considered as part of cladding or layer thickness (Figure 1).

Optical microscopy (OM) and scanning electron microscopy (SEM) were used for the microstructural characterization. The chemical concentration profile was investigated by electron dispersive X-ray spectroscopy (EDXS). The Vickers microhardness profile (HV0.1) was performed at a step of 100 μm, starting from the cladding surface down to the CuBe substrate through the heat-affected zone. The LBC was assessed by a universal tensile test machine. The surface of claddings was indented with a tungsten carbide ball with a diameter of 12 mm. The load force was increased up to 27 kN at a speed of 5 kN min⁻¹ and the load–displacement curves were plotted.

3. Results and Discussion

3.1. Microstructural and Elemental Distribution Analysis

The microstructure of S1–S3 samples is shown in **Figure 2**. First, a single defect-free SS316L layer (S1) was successfully deposited (Figure 2a). The cladding thickness of S1 was 473 μm. The
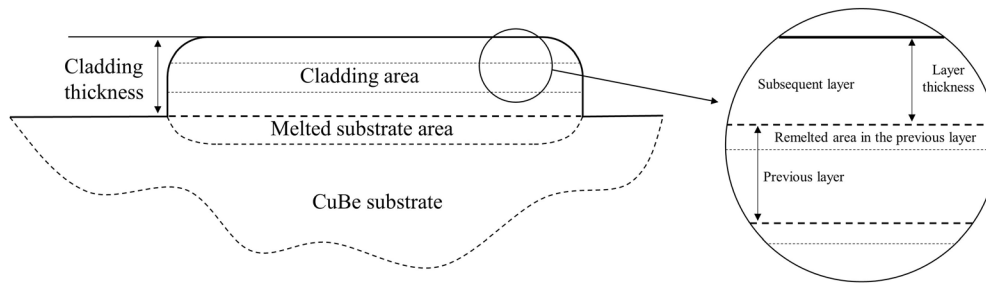
Figure 1. Illustration of geometrical features in transversal cross-section.
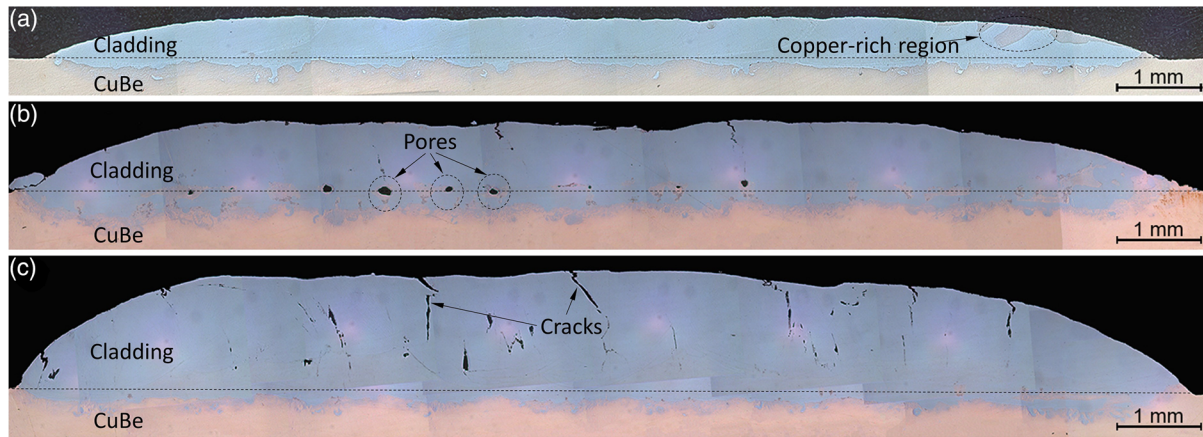

Figure 2. Optical microscopy (OM) micrograph of: a) S1, b) S2, and c) S3.

penetration of cladding into substrate seen in S1 was shallow, which indicated a conduction mode deposition. In addition, several copper-rich zones in a lighter color were easily distinguished in the cladding, which results from the low solubility of copper in iron (Figure 2a). The double-layer sample S2 was then produced (Figure 2b). The cladding thickness of S2 was 820 μm. The parameters for the second H13 layer were optimized attempting to eliminate cracks. However, optimized parameters for minimizing cracking caused spherical pores (S2). To investigate the interfaces of CuBe/SS316L and SS316L/H13, the SEM image

of S2 from CuBe substrate up to H13 cladding was taken, which was shown in **Figure 3**a. The bonding between substrate and cladding was strong. There were turbulence-shaped regions just below the CuBe/SS316L interface, which indicates intensive molten pool convection. Inside the SS316L layer, inverted triangle Cu-rich regions were found, which may imply a keyhole-mode molten pool during the second layer deposition. It was observed that the interface between H13 and SS316L was just above the Cu-rich regions and pores (Figure 2b, 3a, and 4a), which was rather low. The aforementioned phenomenon indicated that a
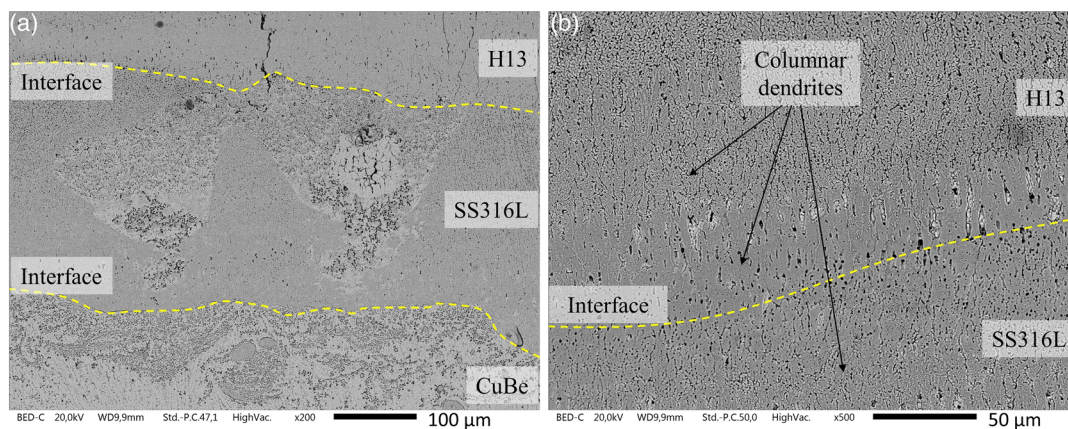

Figure 3. Scanning electron microscopy (SEM) image of: a) S2 and b) the interface area between H13 and SS316L cladding in S2.
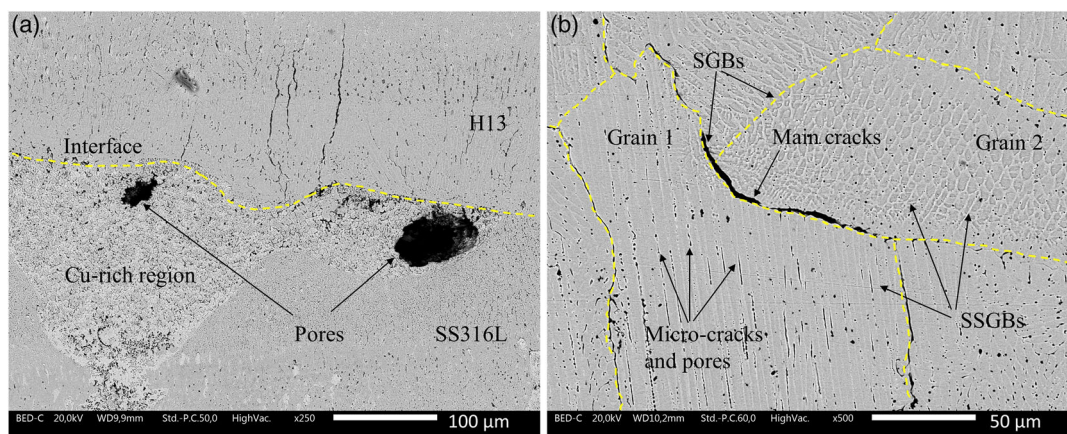
Figure 4. SEM image of: a) pores close to the interface between H13 and SS316L cladding in S2, and b) cracks in H13 cladding of S3.

large part of the SS316L layer was remelted during H13 cladding deposition. For the single-layer (S1) or the first layer (S2) deposition, a large amount of laser energy is reflected due to the low laser absorptivity of the CuBe substrate. Thus, the conduction-mode molten pool was found. However, when depositing the second layer of S2, the first SS316L layer plays as new substrate material with remarkably lower laser reflectivity. Since the energy input was kept the same for the second layer as the first one, the energy input can be high enough to form a keyhole-mode molten pool, which was observed in S2. The difference in laser absorptivity between CuBe and SS316L also explains the low interface of SS316L/H13 in S2. It should be noted that during the parameter optimization it was found that the high energy input was required to eliminate cracks when depositing the second H13 layer. Regarding the microstructure in the interface region between H13 and SS316L, coarser columnar dendrites first grew perpendicular to the interface. The width of interdendritic regions at the H13 cladding bottom was larger than that of the interior interdendritic ones (Figure 3b).

Two types of defects were observed in this work: porosity and cracking. The pores in the near-spherical shape were distributed along with the interface between layers (Figure 2b). With the help of the high magnification image of SEM (Figure 4a), it was distinct that the pores were inside the copper-rich zone. This type of porosity may result from the keyhole mode cladding due to the overabundant energy input. The cracks in S2 were found from

the second layer, have a length of 50–200 μm, and were mostly oriented along the temperature gradient direction (Figure 2b). To investigate the buffer layer number effect and the cracking mechanism, one more layer of SS316L (S3) was added to further reduce the copper concentration in the H13. In S3, cracks also originated in the second layer, even though its material is SS316L rather than H13. Moreover, more and longer cracks were detected, compared to S2 (Figure 2c). It indicates that both H13 and SS316L were susceptible to cracking when depositing as the second layer, even though SS316L has no phase transformation and there is a distinct difference in the alloy elements between the two types of steel. Thus, the aforementioned phenomenon suggests that the cracks observed in this work do not result from phase transformation and alloy elements variation. An SEM high magnification image (Figure 4b) showed that the main cracks were always located at the solidification grain boundaries (SGBs). Inside the grain, there were micro-cracks along solidification subgrain boundaries (SSGBs), which in some cases were the discontinuous micro-pores. These defects inside the grains may result from the insufficient growth of the secondary dendrite arms.[17] The cracks due to solidification are usually located along SGBs. To verify the assumption in terms of the cracking mechanism, the elemental distribution and solidification process will be further discussed in the next content.

The elemental map of Cu and Fe in S3 cladding is shown in **Figure 5**. It was observed that the two SS316L buffer layers
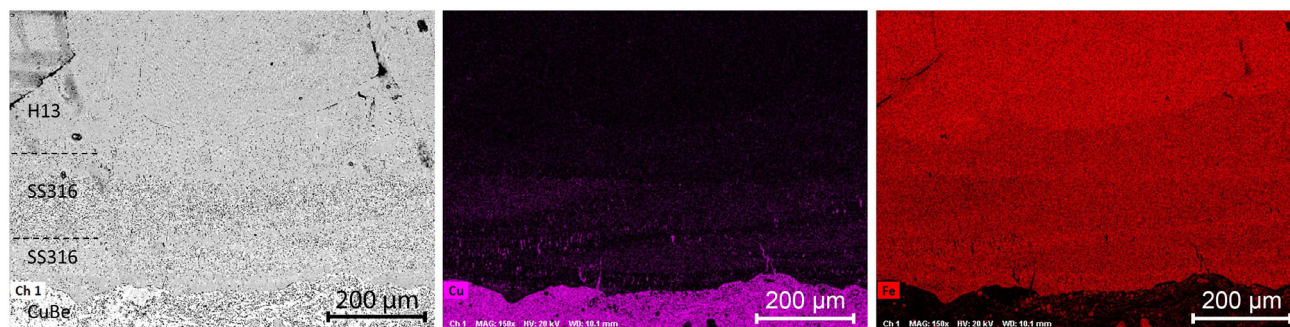

Figure 5. Elemental distribution map of S3 from the CuBe substrate to the H13 cladding.

Table 3. The elemental composition close to the cladding surface of S2 and S3 (wt%).

Sample	Si	V	Cr	Mn	Fe	Ni	Cu	Mo
S2	0.5	0.2	6.5	0.4	63.1	5.2	21.8	2.3
S3	0.6	0.4	10.5	0.7	72.7	5.6	7.8	1.7

strongly reduced the copper concentration in the H13 layer, confirming their efficient barrier effect. To further investigate the copper concentration in the H13 cladding layer, two areas close to the cladding top in S2 and S3 were chosen. The elemental composition in these areas was analyzed and shown in **Table 3**.

The copper concentration in S3 (7.8 wt%) was much lower than in S2 (21.8 wt%). However, the lower copper concentration did not suppress cracking formation, which was counterintuitive. It suggests that the cracking susceptibility may change with the copper concentration in the cladding. The S1 result also implies that a large enough copper concentration may be in favor of cracking elimination considering its dilution is around 20%. To understand the copper distribution at a microscale, an elemental map of S2 was measured by EDXS (**Figure 6**). Copper is more concentrated in the interdendritic region. Combining the fact that the cracks are usually distributed along SGBs or

SSGBs, all observations point out that the cracks may relate to the solidification process. According to the numerous studies of solidification cracking during welding, two main metallurgical factors are dominated: solidification temperature range (STR) and interfacial terminal liquid.[18,19] On one hand, the larger the STR, the higher the cracking susceptibility. On the other hand, sufficient terminal liquid is necessary for grains to move and rearrange themselves to accommodate the tensile strain. Meanwhile, recalling that H13 and SS316L both suffer from cracking, the Fe–Cu binary system rather than other alloy elements should be the main driving force in cracking formation.

To investigate the solidification process in the Fe–Cu binary system, the nonequilibrium solidification paths (**Figure 7**) were plotted by a CALPHAD-methodology-based software Thermo-Calc.

The "classic Scheil model" was used for nonequilibrium calculation, assuming: 1) no diffusion in the solid; 2) infinite diffusion and complete stirring in the liquid, well-fitting the DLMD situation. Two Fe–Cu ratios: 2.9:1 (25.6 wt% Cu) in S2 and 9.3:1 (9.7 wt% Cu) in S3, were chosen for calculation based on the elemental composition in Table 3, corresponding to different cracking susceptibility (low in S2 and high in S3). S2 has a slightly lower STR than S3, around 450 °C, which is still very large promoting a long mushy zone (Figure 7). The mushy zone,
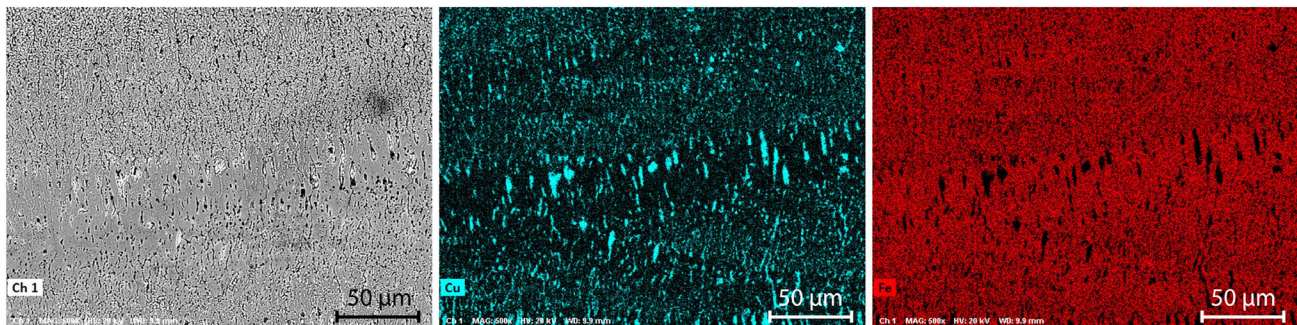

Figure 6. Elemental distribution map of S2 near the cladding interface.
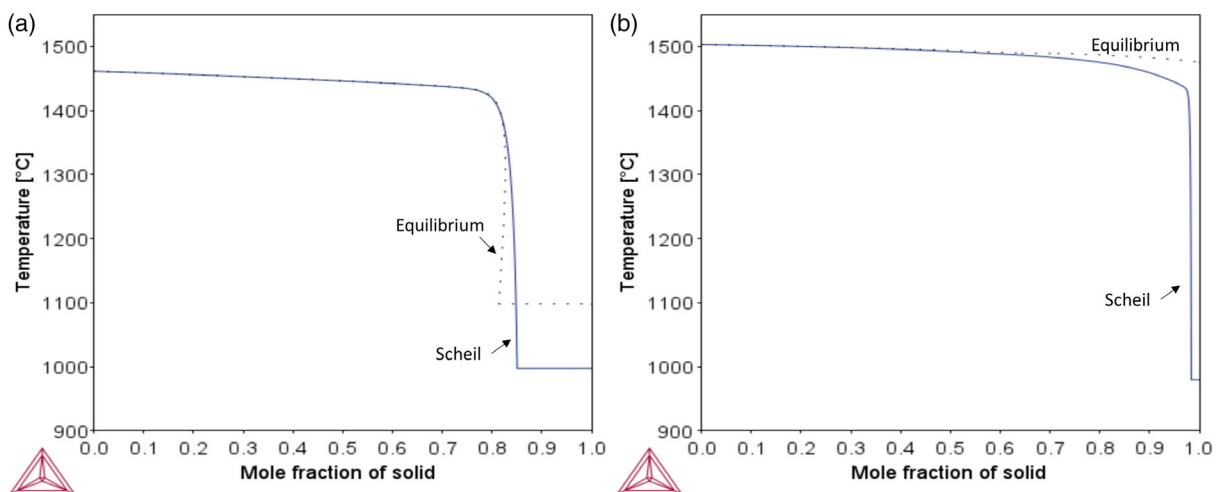

Figure 7. Scheil solidification path based on the Fe–Cu ratio in: a) S2 and b) S3.

2200387 (5 of 8)

ADVANCED
SCIENCE NEWS
www.advancedsciencenews.com

steel
research
international

www.steel-research.de

where the liquid and solidified phases can coexist, is determined by STR. The larger the STR, the longer the mushy zone, where solidified cells or dendrites are separated by liquid films. These liquid films aggravate the cracking tendency due to their rather low strength. Thus, the long mushy zone induced by large STR increases the cracking susceptibility. Nevertheless, the adequate terminal liquid at the last stage of solidification can "heal" cracks by the backfilling effect. Thus, the large amount of terminal liquid existing in S2 suppresses the cracking formation, which explains the relatively fewer cracks in S2 even though the STR is large (Figure 7a). The crack-free S1 verifies the aforementioned cracking mechanism again since the terminal liquid in S1 is abundant due to the large concentration of Cu (Figure 2a). S3 has a large STR and meanwhile limited terminal liquid, which results in a high cracking susceptibility (Figure 7b).

3.2. Microhardness Profile

The microhardness profile of sample S2 shows that the average hardness of H13 cladding was rather low, i.e., close to 400 HV (**Figure 8**a). According to the author's previous work, the microhardness of the H13 cladding by DLMD should reach 800 HV.[12]

Two factors dominate the cladding hardness: the martensite fraction and the copper concentration. First, the martensite fraction was estimated by the property model calculation in the software Thermo-Calc. The model used by Thermo-Calc is based on the quenching condition, which is similar to the DLMD process. The elemental composition of S2 listed in Table 3 was used for the calculation. Note that Cu was not included to reduce the calculated deviation. The calculated martensite fraction is around 99% for S2% and 87% for S3 at room temperature. Such a high fraction of martensite in S2 shows that the relatively low H13 cladding hardness should attribute to the high copper concentration. In terms of S3, the copper contamination and the reduction of martensite fraction both contribute to the slight decrease of H13 cladding hardness compared to S2. Moreover, the cladding hardness varied along the building direction in S2 and S3 (Figure 8a,b). The aforementioned phenomenon may result from the inhomogeneous distribution of copper and defects in the cladding (Figures 2b and 6). As mentioned in Section 3.1, Cu is mainly rejected into SSGBs and SGBs during solidification. Meanwhile, the SGBs can hold more Cu due to their larger size. If measurements take place close to the Cu-rich SGBs, one can easily foresee a low microhardness. The same phenomenon can be seen if a measurement is performed close to defects. The microhardness of the SS316L buffer layer was around 200 HV. The heat-affected zone (HAZ) depth was 2 mm and the lowest microhardness, due to averaging of CuBe substrate, was 120 HV. For S4, the cladding hardness was higher than 550 HV, about 50% higher than that of S2 (Figure 8c). One can imagine that the copper concentration in each layer of S4 is lower than that of S2 due to the multiple remelting processes. Meanwhile, the variation of cladding hardness along the building direction was less due to the more homogenous distribution of copper. The microhardness of the buffer layer was above 300 HV, which was higher than that of S2. HAZ depth of S4 had no obvious difference from that of S2, which was around 2 mm.

3.3. LBC and TC

The LBC of CuBe substrate, S2, S3, and S4 samples was investigated. The load-bearing tests describe the response of the whole system, i.e., the whole sample, rather than only the cladding part. At low load, the system's response is mostly related to the hardness of cladding, while increasing the load the influence of the subsurface layers and substrate becomes more and more evident. The detailed description was reported in the reference.[12] In general, a larger displacement at the same loading force represents the larger plastic deformation and the worse LBC. The displacement versus load force was plotted in **Figure 9**. Here, each originally experimental curve was fitted by the 5-orders polynomial. The R2 for all 3 curves is above 99.95%. The 95% confidence bands were also marked in Figure 9. S3 showed the worst LBC followed by S2, as evidenced by the larger displacement in the whole loading range. At relatively low loads, i.e., up to 10 kN, the LBC of S4 is higher than that of the CuBe substrate. Beyond that load, it started to show the worse LBC compared with CuBe substrate.

The low LBC of S2 and S3 can be ascribed to three distinct effects, namely, 1) the low hardness of the H13 layer; 2) the rather low hardness of the SS316 buffer layer; 3) the softening in the HAZ. Hence, S2 and S3 can be deformed quite easily even under relatively low loads. As increasing the layer number, the cladding microhardness increases as well, which leads to better strength. Thus, one can see the better LBC of S4 at the low load. Note that to minimize cracks, a high energy input was utilized for each layer of cladding in S4. This led to a lower hardness of the
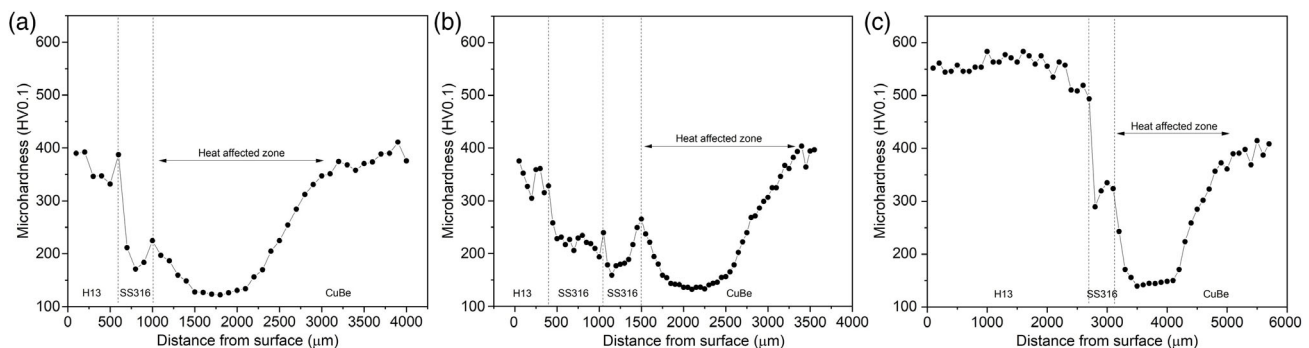

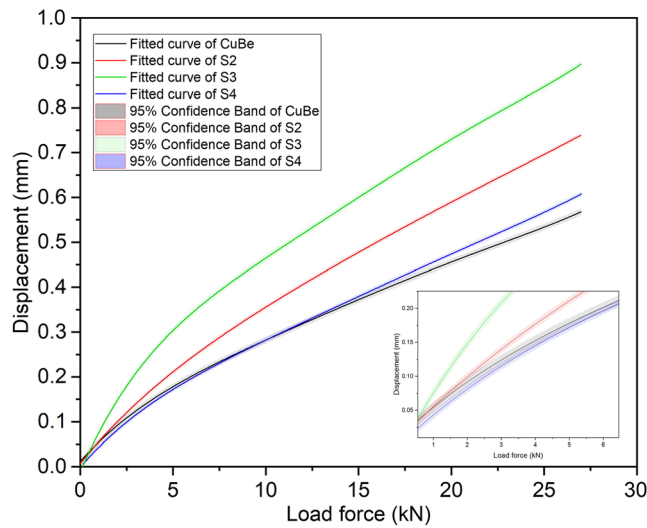**Figure 8.** Microhardness of: a) S2, b) S3, and c) S4.

Figure 9. The load–displacement curves measured by load-bearing capability (LBC) tests.

cladding (550 HV) compared to the ideal one (800 HV).[20,21] Therefore, the choice of a more suitable buffer material, showing less demanding processing parameters, has to be suggested not only to suppress cracking but also to optimize the properties of as-built tool steel cladding.

The TC of samples S2, S3, and S4 at 200 °C was calculated according to the equation proposed by Zhang et al.[16]

$$k_{m} = \frac{k_{t}k_{s}k_{c}(x_{t} + x_{s} + x_{c})}{k_{s}k_{c}x_{t} + k_{t}k_{c}x_{s} + k_{t}k_{s}x_{c}} \quad (1)$$

where k_{m} is the TC of a multi-material structure. x_{t}, x_{s}, and x_{c} are the thickness of H13 tool steel, SS316L buffer, and CuBe substrate, respectively, and k_{t}, k_{s}, and k_{c} are the TC of H13 tool steel, SS316L buffer, and CuBe substrate, respectively. The TC of base materials ($k_{t} = 24$, $k_{s} = 16$, and $k_{c} = 145$ J m^{-1} k^{-1}) were taken from the literature.[22–24] The calculation results were shown in **Table 4**. Moreover, the TC of another sample (S4-1) with the same cladding thickness as S4 but having a thicker CuBe base plate (100 mm) was calculated to approximately simulate the condition in a real mold.

It is clear to see that the thicker cladding weakens the TC of the whole cladding system. Around 47% reduction was observed in S4 where the cladding thickness ratio was above 13%. However, it must be mentioned that the matrix of a mold is much thicker than the substrate used in this work. For example, by reducing

the cladding to substrate thickness ratio to 2.7%, as in sample S4-1, the TC reduction induced by cladding was dramatically suppressed into a reasonable range (<18%). The TC and LBC results reported in this article demonstrate that a cladding system can achieve a very good combination of these properties. Nevertheless, they could be tuned according to the specific cladding thickness for a specific position in the mold, thanks to the flexibility offered by DLMD.

4. Conclusion

H13 cladding on CuBe alloy substrate was deposited by DLMD using a buffer layer strategy to try to reduce cracking. The SS316L was chosen as the buffer material due to its high ductility and good weldability. Defect-free single-layer SS316L on CuBe substrate was deposited. The multi-layer systems (SS316 + H13, and 2×SS316 + H13) showed cracks. The main results of the characterization carried out in this work can be summarized in the following points: 1) Two types of defects were observed: porosity and cracking. The pores were located along with the interface between cladding layers, as a result of the keyhole mode cladding. The cracks preferentially grew in the dendrite growth direction and were located at SGBs and SSGBs. These cracks are attributed to the solidification process. Two main factors: solidification temperature range and terminal liquid, dominate the cracking susceptibility. Decreasing the solidification temperature range or increasing the amount of terminal liquid can reduce the cracking tendency; 2) The cladding microhardness of the double-layer system (S2) was rather low due to the large copper concentration. Adding one more SS316L layer (S3) slightly reduces the H13 cladding microhardness due to the less martensite fraction. Meanwhile, the LBC of S3 showed the worst due to the low average microhardness of cladding and HAZ; 3) When increasing the layer number, S4 (1-layer SS316L + 4-layer H13) had the better LBC in the low loading range compared with the CuBe substrate due to the high average cladding microhardness. Above 10 kN, S4 showed worse LBC due to the low strength of SS316 cladding and HAZ. The increase in the layer number raised the cladding hardness and LBC simultaneously. A 3% cladding to substrate ratio can remain more than 80% TC of a whole cladding system.

This work confirms that both tool steel and stainless steel are highly susceptible to solidification cracking when depositing on copper alloys. Thus, to eliminate cracking and improve the cladding strength simultaneously, another proper buffer material should be found. Moreover, controlling the cladding thickness as thin as possible is beneficial for keeping the high TC of the whole cladding system. Thus, the cladding strength needs to be further improved based on this work. Other factors leading to solidification cracking needs to be further investigated in detail.

Table 4. Values of TC calculated by the Zhang model.[16]

Sample	x_{t} [mm]	x_{s} [mm]	x_{c} [mm]	Cladding thickness [mm]	TC [J m^{-1} k^{-1}]
S2	0.35	0.47	20	0.82	116.1
S3	0.44	0.94	20	1.38	104.5
S4	2.26	0.47	20	2.73	76.1
S4-1	2.26	0.47	100	2.73	120.8

Conflict of Interest

The authors declare no conflict of interest.

Data Availability Statement

The data that support the findings of this study are available from the corresponding author upon reasonable request.

Keywords

additive manufacturing, molding injection, simulation, steel properties, tools

[1] D. V. Rosato, M. G. Rosato, *Injection Molding Handbook*, Springer Science & Business Media, New York, NY **2012**.

[2] S. Schneider, S. Bajohr, F. Graf, T. Kolb, *ChemBioEng Rev.* **2020**, *5*, 30.

[3] F. F. Noecker, J. N. DuPont, *presented at Inter. Cong. on App. of Lasers & Electro-Optics*, Laser Institute of America, Scottsdale, Arizona, USA, October **2002**.

[4] J. O. Carlsson, P. M. Martin, *Handbook of Deposition Technologies for Films and Coatings*, William Andrew, Kidlington, Oxford, UK **2002**.

[5] N. Shamsaei, A. Yadollahi, L. Bian, S. M. Thompson, *Addit. Manuf.* **2015**, *8*, 12.

[6] S. M. Thompson, L. Bian, N. Shamsaei, A. Yadollahi, *Addit. Manuf.* **2015**, *8*, 36.

[7] C. Han, Q. Fang, Y. Shi, S. B. Tor, C. K. Chua, K. Zhou, *Adv. Mater.* **2020**, *32*, 1903855.

[8] B. Li, C. Han, C. W. J. Lim, K. Zhou, *Mater. Sci. Eng., A* **2022**, *829*, 142101.

[9] A. Bandyopadhyay, B. Heer, *Mater. Sci. Eng., R.* **2018**, *129*, 1.

[10] M. K. Imran, S. H. Masood, M. Brandt, S. Bhattacharya, J. Mazumder, *Mater. Sci. Eng., A* **2011**, *528*, 3342.

[11] M. K. Imran, S. H. Masood, M. Brandt, *Lasers Manuf. Mater. Process.* **2015**, *2*, 242.

[12] M. Pellizzari, Z. Zhao, P. Bosetti, M. Perini, *Surf. Coat. Technol.* **2022**, *432*, 128084.

[13] D. K. Kim, W. Woo, E. Y. Kim, S. H. Choi, *J. Alloys Compd.* **2019**, *774*, 896.

[14] M. K. Imran, S. H. Masood, M. Brandt, S. Bhattacharya, S. Gulizia, M. Jahedi, J. Mazumder, *Surf. Coat. Technol.* **2012**, *206*, 2572.

[15] X. Zhang, T. Pan, Y. Chen, L. Li, Y. Zhang, F. Liou, *J. Mater. Sci. Technol.* **2021**, *80*, 100.

[16] X. Zhang, C. Sun, T. Pan, A. Flood, Y. Zhang, L. Li, F. Liou, *Addit. Manuf.* **2020**, *36*, 101474.

[17] E. Chauvet, P. Kontis, E. A. Jägle, B. Gault, D. Raabe, C. Tassin, J. J. Blandin, R. Dendievel, B. Vayre, S. Abed, G. Martin, *Acta Mater.* **2018**, *142*, 82.

[18] S. Kou, *Welding Metallurgy*, John Wiley & Sons, Hoboken, NJ **2002**.

[19] J. C. Lippold, S. D. Kiser, J. N. DuPont, *Welding Metallurgy and Weldability of Nickel-Base Alloys*, John Wiley & Sons, Hoboken, NJ **2011**.

[20] H. L. Wei, T. Mukherjee, W. Zhang, J. S. Zuback, G. L. Knapp, A. De, T. DebRoy, *Prog. Mater. Sci.* **2021**, *116*, 100703.

[21] T. DebRoy, H. L. Wei, H. L. Zuback, T. Mukherjee, J. W. Elmer, J. O. Milewski, W. Zhang, *Prog. Mater. Sci.* **2018**, *92*, 112.

[22] UDDEHOLM, https://www.uddeholm.com/us/en-us/products/uddeholm-coolmould/ (accessed: September 2017).

[23] C. Francois, *Materials Handbook*, Springer-Verlag, London, UK **2008**.

[24] H. E. Boyer, T. L. Gall, *Metals Handbook*, ASM International, OH **1985**.

2200387 (8 of 8)